bioRxiv preprint doi: https://doi.org/10.1101/2023.01.09.523298; this version posted January 9, 2023. The copyright holder for this preprint (which was not certified by peer review) is the author/funder, who has granted bioRxiv a license to display the preprint in perpetuity. It is made available under aCC-BY-NC-ND 4.0 International license.

Population-level interactions among PV, SOM, and Pyramidal neurons in cortex

Christian T. Potter[1,2,+], Constanza D. Bassi[1,2+], Caroline A. Runyan[1,2,*]
[1]Department of Neuroscience, University of Pittsburgh
[2]Center for the Neural Basis of Cognition

[+]These authors contributed equally
[*]Corresponding Author: runyan@pitt.edu

Abstract

The inhibitory neuron population of the cortex can be subdivided into multiple cell classes with highly specialized local circuitry, gene expression, and response properties. PV and SOM neurons are two nonoverlapping cell classes with distinct but interacting functional roles, that depend on brain state. Here, we have applied a simple approach to identify PV, SOM, and putative pyramidal (Pyr) neurons within the same mice. We imaged their spike-related calcium activity in the posterior parietal cortex (PPC) while mice voluntarily ran on a spherical treadmill. We then related the activity of the simultaneously imaged neurons to each other, revealing that the activity of all inhibitory neurons was positively correlated compared to the activity within the Pyr population, and correlations were strongest among neurons of the same type. Furthermore, these activity relationships decayed with distance when comparing Pyr and inhibitory neurons, but not PV and SOM neurons. Finally, we identified coordinated activity events that were mostly restricted to either the PV or the SOM population, and used dimensionality reduction tools to reveal that these PV and SOM events were associated with different activity states in the Pyr population. This methodology will be useful to study population-level interactions across cell types in cortical circuits, and how they depend on behavioral state and task engagement.

Introduction

Inhibitory interneurons powerfully influence local processing in the cortex by shaping response properties, controlling the timing of responses, balancing excitation, and more (Wehr and Zador, 2003; Cardin et al., 2009; Sohal et al., 2009; Adesnik et al., 2012; Atallah et al., 2012; Wilson et al., 2012; Pi et al., 2013; Chen et al., 2015; Kato et al., 2017; Veit et al., 2017; Rikhye et al., 2021). A diverse population, inhibitory interneurons can be subdivided into highly specialized classes based on gene expression profiles, electrophysiological properties, and local connectivity patterns (Tremblay et al., 2016). A useful subdivision is based on the expression of somatostatin (SOM), parvalbumin (PV), and vasoactive intestinal protein (VIP), which defines three non-overlapping cell classes. These are not homogeneous cell populations, as each can be further subdivided based on expression of other proteins, local connectivity, and function. Still, specialized connectivity within each population allows PV, SOM, and VIP neurons to in general play different functional roles in cortical circuits (Figure 1A). PV neurons receive similar

bioRxiv preprint doi: https://doi.org/10.1101/2023.01.09.523298; this version posted January 9, 2023. The copyright holder for this preprint (which was not certified by peer review) is the author/funder, who has granted bioRxiv a license to display the preprint in perpetuity. It is made available under aCC-BY-NC-ND 4.0 International license.

feedforward excitation as neighboring pyramidal neurons, with which they form strong reciprocal connections (Yoshimura and Callaway, 2005; Hofer et al., 2011; Znamenskiy et al., 2018), allowing PV neurons to divisively normalize excitatory responses to control response gain (Atallah et al., 2012; Wilson et al., 2012). SOM neurons are driven more weakly by feedforward excitation, instead pooling excitation laterally to provide a source of surround suppression that is fundamental to local circuits, and to sculpt the tuning profiles of excitatory neurons (Adesnik et al., 2012; Kato et al., 2017).

Inhibitory neurons are also key in mediating the state dependence of cortical processing. For example, SOM neurons are highly sensitive to changes in neuromodulatory input (Fanselow et al., 2008; Adesnik et al., 2012; Chen et al., 2015). Locally, although SOM neurons do monosynaptically inhibit excitatory neurons, they also participate in two disinhibitory microcircuits. In a unidirectional disinhibitory circuit, SOM neurons inhibit PV cells, so that the response gain in local excitatory neurons can be scaled up or down (Pfeffer et al., 2013), and enhance the response reliability of excitatory neurons (Rikhye et al., 2021). SOM and VIP neurons synaptically inhibit each other (Pi et al., 2013; Pfeffer et al., 2022), adding another layer of local control of excitatory response tuning and timing. Furthermore, the interactions of SOM neurons with PV and with VIP neurons increases the number of states achievable by local networks (Wang and Yang, 2018), enhancing the flexibility of cortical processing across behavioral states. To understand the roles that inhibitory neurons play in shifting and shaping local processing, their activity must be simultaneously monitored.

To characterize the function of specific inhibitory cell classes, experimenters often cross transgenic mouse line expressing Cre in a specific inhibitory cell class (e.g. PV-Cre) with a floxed line (e.g. Ai14) to express a fluorescent reporter (e.g. tdTomato) in the cell type of interest (Hofer et al., 2011). A calcium indicator such as GCaMP is then expressed in all neurons for *in vivo* characterization of the cell type expressing the fluorescent reporter, and comparing its activity profiles to those of the rest of the neural population. These methods can be applied to multiple brain areas, and in mice performing perceptual tasks, to characterize the tuning and the functional interactions between one neuron type and the rest of the population (Kuchibhotla et al., 2016; Garcia-Junco-Clemente et al., 2017; Dipoppa et al., 2018). However, using this approach to compare functional properties across inhibitory and excitatory neuron types would require comparison of neural activity recorded in different animals, and so functional interactions between inhibitory neuron types cannot be examined. This severely limits the ability to understand neural activity on individual trials, given that variability in its evolution is explained by interactions across all cell types. Further, the activity of neurons across the cortex can be significantly modulated by idiosyncratic motor behaviors and shifting arousal states (Musall et al., 2019; Stringer et al., 2019), leading to individual differences in neural activity patterns. A more powerful approach would allow the simultaneous recording of multiple cell types. This has been accomplished in a few labs (Kerlin et al., 2010; Poort et al., 2015; Bugeon et al., 2022;

bioRxiv preprint doi: https://doi.org/10.1101/2023.01.09.523298; this version posted January 9, 2023. The copyright holder for this preprint (which was not certified by peer review) is the author/funder, who has granted bioRxiv a license to display the preprint in perpetuity. It is made available under aCC-BY-NC-ND 4.0 International license.

Condylis et al., 2022) by performing *in vivo* imaging, perfusing the mouse, slicing the brain, staining for cell-type specific proteins, and registering the stained tissue to the *in vivo* images. This is a technically challenging process that is not easily applied.

Here, we have applied simpler approach to identify two distinct inhibitory cell classes, PV and SOM neurons *in vivo*, by expressing spectrally separable red fluorescent proteins in the two interneuron populations. We then virally expressed GCaMP in the full neural population, considering neurons not expressing the red fluorophores to be putative pyramidal neurons. We then used calcium imaging to relate the activity of PV, SOM, and putative pyramidal neurons, imaged together in the same mice. Using this approach, we have uncovered distinct activity states in the pyramidal population that are associated with coordinated events in the SOM and PV populations.

Results

1.0 Validation of spectral separation to distinguish tdTomato from mCherry expressing cells

In principle, tdTomato and mCherry are separable fluorophores, based on their excitation spectra (Drobizhev et al., 2009). To test for this possibility in vivo, we injected a Cre-dependent tdTomato construct and a Flp-dependent mCherry construct in adjacent but physically separate, locations in the posterior parietal cortex of SOM-Flp (+/-) x PV-Cre (+/-) mice (Figure 1A). The injection sites could then be imaged simultaneously *in vivo* with a two-photon microscope. As expected from the known two-photon excitation spectra of tdTomato and mCherry (Drobizhev et al., 2009), the sites' relative intensity depended on the excitation wavelength of the laser. At ~800 nm, the tdTomato site was nearly invisible, while the mCherry site was well-defined. Near 1040 nm, both sites were visible (Figure 1B). At intermediate wavelengths, we observed more subtle differences in relative intensity (Figure 1C).

We hypothesized that the full excitation intensity profiles of mCherry and tdTomato could be leveraged to accurately distinguish populations of neurons expressing these fluorophores. To do so, we collected images while exciting the neighboring tdTomato- and mCherry-expressing sites at wavelengths of 20 nm increments from 780 to 1100 nm and at a range of excitation powers (0 to 275 mW), excluding the 1020 and 1060 nm wavelengths that were blocked by the optical configuration of the microscope (see Methods). After registering and segmenting these stacks of images, an intensity value for each ROI at each excitation wavelength and power was collected and fed into a clustering algorithm (k-means, see Methods, Figure 1D). We reasoned that some combinations of excitation wavelengths, those with differing mCherry and tdTomato excitation, would be better able to distinguish the two fluorophores, while some excitation wavelengths would be uninformative or even add noise. We applied the clustering algorithm to all possible combinations of excitation parameters, and tested its performance in identifying known

bioRxiv preprint doi: https://doi.org/10.1101/2023.01.09.523298; this version posted January 9, 2023. The copyright holder for this preprint (which was not certified by peer review) is the author/funder, who has granted bioRxiv a license to display the preprint in perpetuity. It is made available under aCC-BY-NC-ND 4.0 International license.

mCherry- and tdTomato-expressing neurons (146 known mCherry+ neurons, 180 known tdTomato+ neurons from 6 fields of view in two mice, Figure 1E). Indeed, our clustering method based on relative intensities across excitation wavelengths was 100% accurate in classifying neurons as tdTomato+ or mCherry+ in the 'best' wavelength permutations shown in Figure 1E. Clustering based on the best wavelength combinations outperformed clustering based on all wavelengths (compare cluster separability of the dotted purple line in Figure 1E). Finally, to identify a cut-off for well-classified ROIs, we examined the cluster separability (silhouette scores) resulting from clustering based on sub-optimal wavelength combinations. In these cases, but not when using optimal wavelength combinations, some neurons were misclassified. We used the distribution of misclassified silhouette scores to choose a threshold for discarding ambiguous red ROIs in subsequent datasets and analyses.

bioRxiv preprint doi: https://doi.org/10.1101/2023.01.09.523298; this version posted January 9, 2023. The copyright holder for this preprint (which was not certified by peer review) is the author/funder, who has granted bioRxiv a license to display the preprint in perpetuity. It is made available under aCC-BY-NC-ND 4.0 International license.

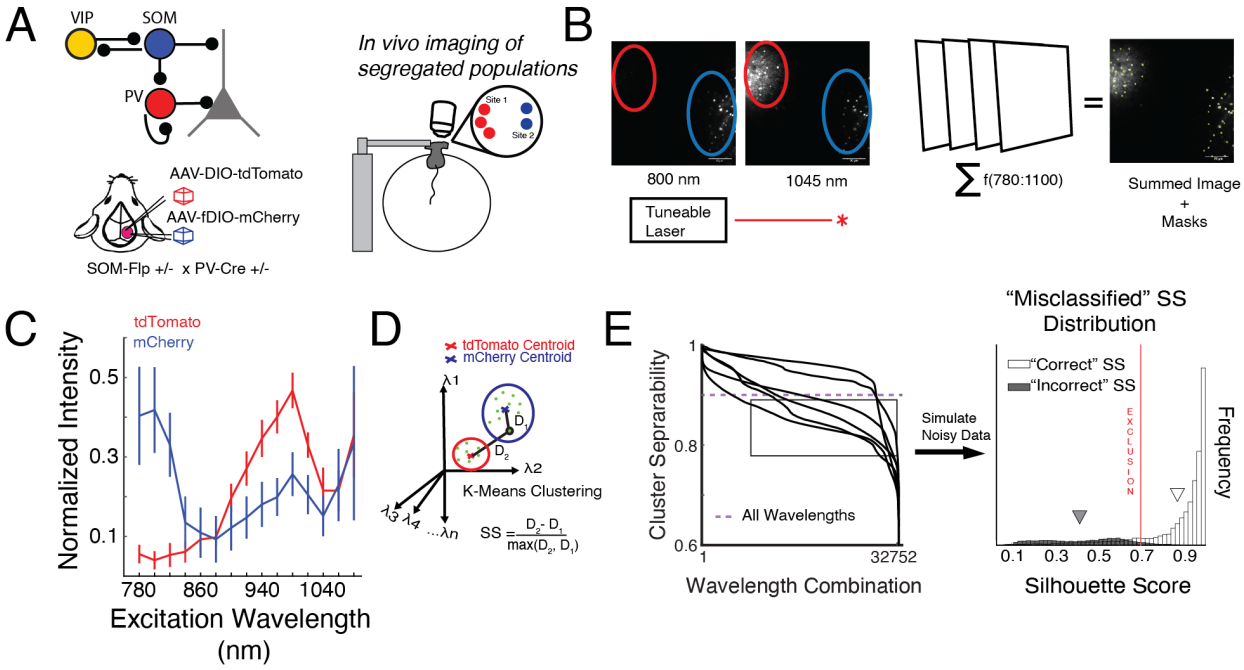

Figure 1: Validation of methods to spectrally separate mCherry and tdTomato expressed in PV and SOM neurons in vivo.
(A) SOM-Flp x PV-Cre mice received two adjacent but physically segregated injections of a Cre-dependent tdTomato and a Flp-dependent mCherry construct. For in vivo two-photon imaging, mice were head fixed on a spherical treadmill.
(B) A field of view was selected to include both the tdTomato (red circle) and mCherry (blue circle) injection sites. A series of images was collected, spanning excitation wavelengths from 780 to 1100 nm. The mCherry site, but not the tdTomato site was visible with 800 nm (left), while both sites were visible with 1045 nm excitation. ROIs were drawn over the cell bodies of the neurons to select pixels for analysis.
(C) Mean normalized intensity of tdTomato ROIs (red) and mCherry ROIs (blue), at all excitation wavelengths. Error bars indicate one standard deviation from the mean.
(D) Schematic of the clustering strategy to identify tdTomato+ and mCherry+ neurons, based on their excitation spectra: K-means clustering was applied to the fluorescence of all mCherry and tdTomato ROIs collected at all possible combinations of excitation wavelengths. For each combination, cluster separability was assessed by computing silhouette scores, which compared each ROI's distance to the centroids of the two clusters.
(E) (Left) Cluster separability, the mean silhouette score of all ROIs, of each permutation of the 15 excitation wavelengths, ordered from best to worst clustering performance. Each line is the cluster separability of a different control imaging dataset (n = 6). Dashed purple line: Cluster separability when using all wavelength combinations to perform clustering. (Right) To simulate the distribution of silhouette scores in suboptimal conditions, where mCherry and tdTomato might be more difficult to distinguish from each other, we selected a range of less optimal wavelength combinations (indicated by the rectangle in the plot on the left). We then assessed the accuracy of cluster identity for each ROI, and compared the distribution of silhouette scores for correctly (white) and incorrectly (gray) classified ROIs. The means of each distribution are indicated by the triangles. An exclusion threshold was drawn 2 sd above the mean of the distribution of incorrect SS's (red line), and used in subsequent experiments to discard ROIs with potentially ambiguous identities. Note that at optimal wavelength combinations, no ROIs were misclassified.

2.0 Simultaneous imaging of SOM, PV, and Pyr neurons in layer 2/3 to study population-level interactions across cell types

Having validated our method for spectral separation of mCherry and tdTomato *in vivo* using physically separated control expression sites (Figure 1), we then applied the approach to identify intermingled somatostatin-expressing neurons that were mCherry+ (SOM), parvalbumin neurons that were tdTomato+ (PV), and putative pyramidal neurons that were negative for both red fluorophores (Pyr). All three neuron types expressed GCaMP6f, a genetically encoded calcium

bioRxiv preprint doi: https://doi.org/10.1101/2023.01.09.523298; this version posted January 9, 2023. The copyright holder for this preprint (which was not certified by peer review) is the author/funder, who has granted bioRxiv a license to display the preprint in perpetuity. It is made available under aCC-BY-NC-ND 4.0 International license.

indicator (Chen et al., 2013) to monitor and relate their ongoing activity fluctuations (3 mice, 6 imaging fields of view). During imaging sessions, mice were headfixed under a two-photon microscope, and voluntarily ran on a spherical treadmill (Figure 1A). In a typical field of view, 40±18 PV, 13±7 SOM, and 291±158 Pyr neurons (mean ± s.d.) could be identified by collecting the series of images across excitation wavelengths at the beginning of each imaging session and applying our clustering approach (Figure 2A). For functional imaging, the excitation laser was tuned to 920 nm. GCaMP fluorescence timeseries were extracted for each cell's ROI, dF/F was calculated, and a deconvolution algorithm applied (Figure 2B). All analyses were performed on both dF/F and deconvolved activity.

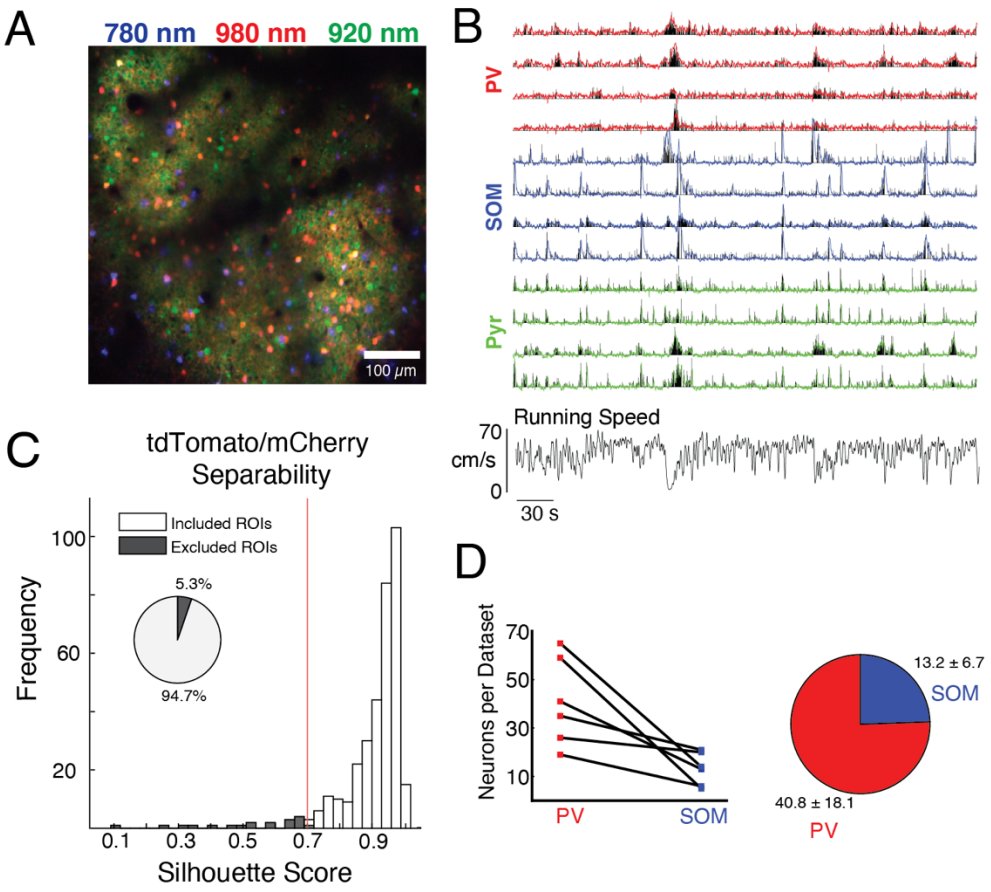

Figure 2: Distinguishing intermingled SOM and PV neurons using spectral separation.
(A) Example field of view from layer 2/3 of PPC. The image is a merge of red fluorescence collected using 780 nm excitation (blue, visualizes mCherry+/SOM+ neurons) and 980 nm (red, visualizes both mCherry+/SOM+ and tdTomato+/PV+ neurons), and green fluorescence collected using 920 nm excitation (green, visualizes all neurons). Neurons with green but not red fluorescence were considered putative pyramidal neurons (Pyr).
(B) GCaMP fluorescence changes in a subset of the PV, SOM, and Pyr neurons in the field of view in A (colored traces: red/PV, blue/SOM, and green/Pyr). Black: estimated spike rates. Bottom: Time-aligned running speed of the mouse.
(C) Distribution of tdTomato/mCherry cluster separability (silhouette scores) for all red neurons. 0.7 was selected as an exclusion threshold, based on our estimate of noisy data in Figure 1E (red vertical line).
(D) Neurons classified as PV+/tdTomato+ and SOM+/mCherry+ in all datasets.

3.0 Relating activity across cell types (pairwise)

bioRxiv preprint doi: https://doi.org/10.1101/2023.01.09.523298; this version posted January 9, 2023. The copyright holder for this preprint (which was not certified by peer review) is the author/funder, who has granted bioRxiv a license to display the preprint in perpetuity. It is made available under aCC-BY-NC-ND 4.0 International license.

The activity of inhibitory interneurons is strongly correlated with the activity of other inhibitory interneurons of the same subtype, across cortex (Karnani et al., 2016; Khan et al., 2018a; Knoblich et al., 2019; Bugeon et al., 2022; Khoury et al., 2022). To determine whether these patterns of activity relationships between pairs of individual SOM, PV, and Pyr neurons hold in mouse PPC, we computed pairwise Pearson correlations, after discounting the effects of running velocity on each neuron's activity (see Methods). When examining the sign and magnitude of these correlations in each imaging dataset, we observed a diversity of relationships for all cell type pairs examined (Figure 3A). Pairs of neurons could be negatively (Figure 3B-C) correlated, positively correlated, or uncorrelated with each other (Figure 3A-F). This diversity of correlations among inhibitory neuron types is unsurprising, given the complexity of local microcircuitry, which includes gap junctions among neurons of the same type (Galarreta and Hestrin, 1999; Hu and Agmon, 2015), inhibitory synapses among PV pairs and PV-SOM pairs (Pfeffer et al., 2013), and likely overlapping recurrent excitatory connectivity (Adesnik et al., 2012; Kato et al., 2017). The distribution of pairwise correlations among cell type pairs is consistent with these patterns: SOM-SOM, and to a lesser extent PV-PV and SOM-PV, pairs tend to be strongly and positively correlated (Figure 3F). Of all the cell type combinations, the least correlated pairs were the Pyr-Pyr pairs. Interestingly, the predominance of negative correlations also differed across cell types, with interneuron pairs being more negatively correlated than Pyr-Pyr pairs Figure (3F). See Table 1 for statistics.

The spatial scales of local of synaptic connection probability and pairwise functional interactions are key determinants of the properties of local network dynamics (Huang et al., 2019). Local Pyr-Pyr functional interactions and synaptic connection probability decay with distance (Song et al., 2005; Levy and Reyes, 2012). The properties of cell-type specific inhibitory-inhibitory interactions in local circuits are less well understood. To determine the spatial scale of local inhibitory functional interactions, we examined the relationship between intersomatic distance and pairwise activity correlation. The magnitude of correlations depended on intersomatic distance for some cell type pairs, but not others (Figure 3G). As expected from their synaptic connectivity profiles (Song et al., 2005; Levy and Reyes, 2012), correlations between Pyr-Pyr and Pyr-PV pairs decayed with distance (Figure 3G), and SOM-Pyr correlations also decayed with distance, but more slowly. Interestingly, SOM-SOM, PV-PV and SOM-PV correlations did not depend on distance, at least at the spatial scale examined here (0-800 μm). See Table 2 for statistics.

bioRxiv preprint doi: https://doi.org/10.1101/2023.01.09.523298; this version posted January 9, 2023. The copyright holder for this preprint (which was not certified by peer review) is the author/funder, who has granted bioRxiv a license to display the preprint in perpetuity. It is made available under aCC-BY-NC-ND 4.0 International license.

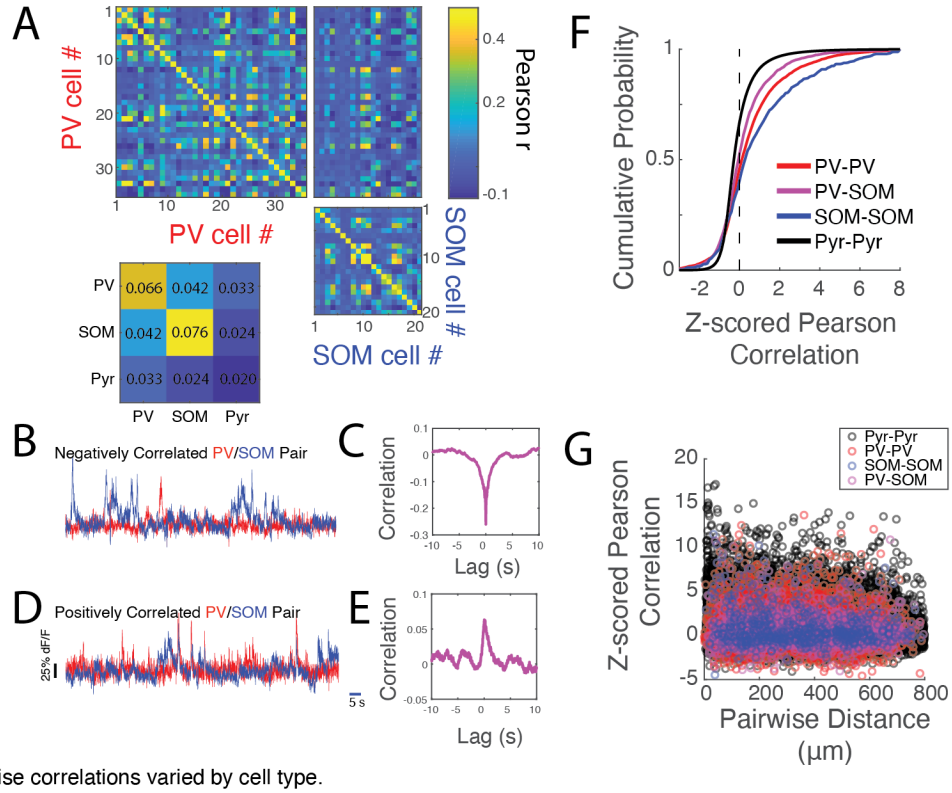

Figure 3: Pairwise correlations varied by cell type.
(A) Pearson correlations between PV and SOM cells in an example dataset, computed after discounting the effects of running on each neuron's activity. Lower left: average Pearson correlation for all cell type combinations, across all datasets (n = 6 datasets).
(B) dF/F timeseries of a pair of negatively correlated PV (red) and SOM (blue) neurons, from the dataset in A.
(C) Cross correlation function of the pair of negatively correlated neurons in B, computed across time lags spanning 10 s in each direction.
(D) dF/F timeseries of a pair of positively correlated PV (red) and SOM (blue) neurons, from the dataset in A.
(E) Cross correlation function of the pair of positively correlated neurons in D, computed across time lags spanning 10 s in each direction.
(F) Cumulative distributions of the pairwise correlations of PV-PV, PV-SOM, SOM-SOM, and Pyr-Pyr cell types. All cell type pair combinations were significantly different from each other ($p<0.0001$), except for PV-PV and SOM-SOM, which were similarly strongly correlated. See Table 1 for full statistics and all cell type combinations.
(G) Pearson correlation plotted against the distance between neuron pairs.

4.0 Population-level interactions across cell types

Combining our spectral separation method with two-photon imaging, we could now examine population-level interactions between cell types, for instance by taking advantage of dimensionality reduction tools (Cunningham and Yu, 2014). As has been already observed, and we have again shown in Figure 3, inhibitory interneurons tend to be strongly correlated with other inhibitory neurons of the same type. Indeed, even a quick examination of the raw activity of SOM and PV neurons in our datasets illustrates multi-neuron activity events within the SOM and PV populations, that are not always shared across cell types (Figure 2B).

bioRxiv preprint doi: https://doi.org/10.1101/2023.01.09.523298; this version posted January 9, 2023. The copyright holder for this preprint (which was not certified by peer review) is the author/funder, who has granted bioRxiv a license to display the preprint in perpetuity. It is made available under aCC-BY-NC-ND 4.0 International license.

We hypothesized that these SOM and PV subpopulation events are related to, and maybe even driving, the activity state of the local Pyr population. To study the local population activity associated with these activity patterns, we identified PV and SOM population activity events in the averaged population activity for each subtype using a peak-finding algorithm (Figure 4A), and restricted the analyzed events within each population to times that the other inhibitory population's activity was low (Figure 4A-B, N = 25 $\pm$ 8 PV population events per dataset, N = 30 $\pm$ 7 SOM population events per dataset). We first examined the average activity within each cell type population during SOM and PV events. Pyr activity was elevated during both types of events (Figure 4C), while, unsurprisingly given the definition of the events, PV activity was relatively low during SOM events and vice versa (Figure 4D-E). Next, to compare the activity of the three populations more directly, we overlaid their activity during PV (Figure 4F) and SOM (Figure 4G) events. Interestingly, activity in the three cell types increased simultaneously at the onset of PV population events, while PV and Pyr activity both preceded SOM activity during SOM population events.

To determine whether the pattern of activity across the Pyr population differed during SOM and PV events, we used dimensionality reduction methods (Cunningham and Yu, 2014) to determine whether PV and SOM events were associated with movement of activity to different locations in population activity state space. Visual inspection of these Pyr population activity trajectories revealed that distinct patterns of activity accompanied PV and SOM events (Figure 4H). Next, we used factor analysis to compare the dimensionality of shared variability across the Pyr population during PV and SOM events. Shared variability was strongest in the first dimension, during both types of events, though the eigenvalues decayed gradually in higher dimensions during both types of events (Figure 4I). Shared variability in the first four dimensions was stronger during PV events than SOM events (Figure 4I, stats), suggesting that SOM and PV population events are associated with different network states: when SOM neurons are highly active, Pyr activity is more decorrelated.

bioRxiv preprint doi: https://doi.org/10.1101/2023.01.09.523298; this version posted January 9, 2023. The copyright holder for this preprint (which was not certified by peer review) is the author/funder, who has granted bioRxiv a license to display the preprint in perpetuity. It is made available under aCC-BY-NC-ND 4.0 International license.

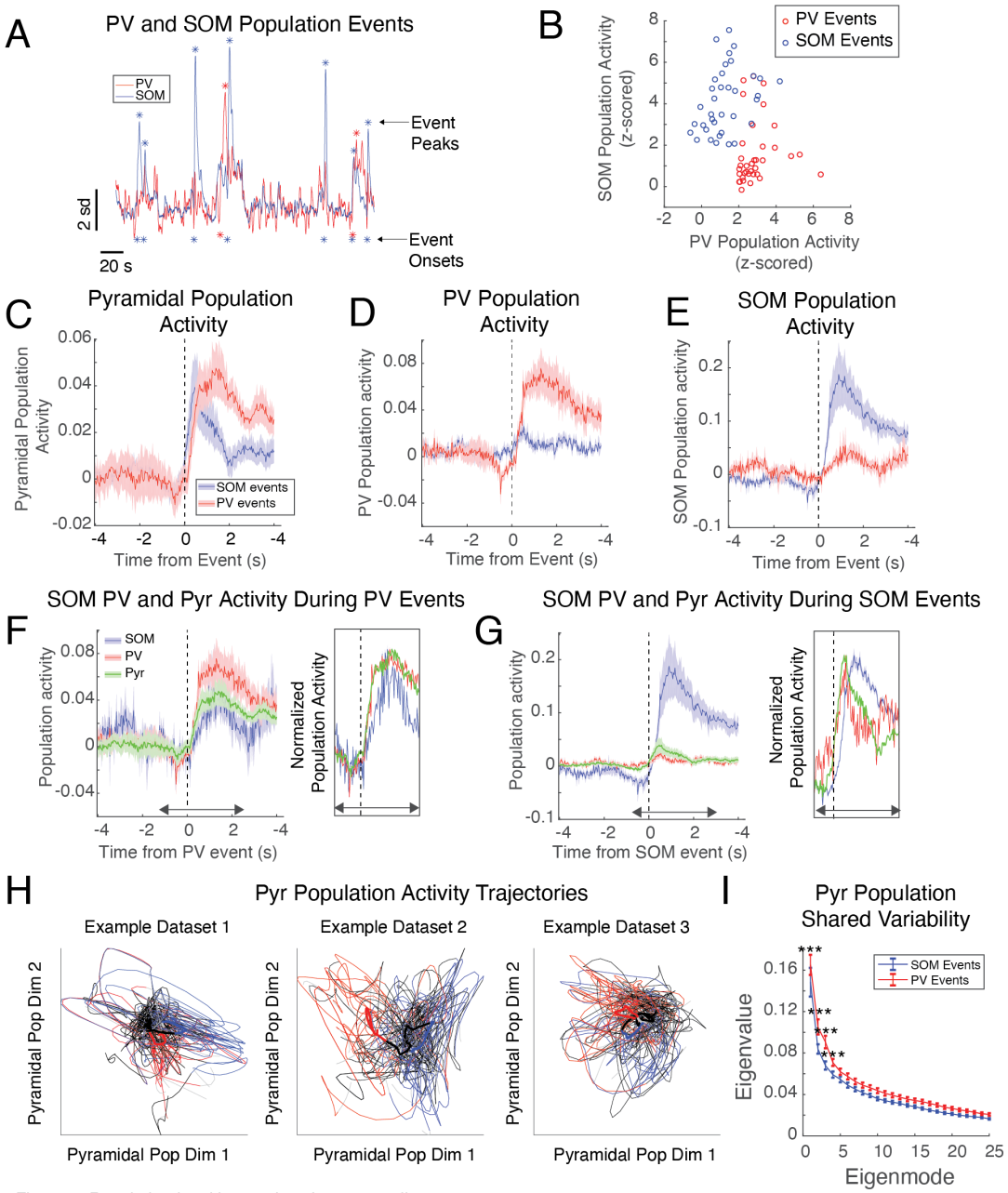

Figure 4: Population-level interactions between cell types.
(A) Population activity in simultaneously imaged SOM (blue) and PV (red) neurons (z-scored and averaged across neurons). Coordinated activity events were defined as peaks of activity that were unique to one population. Asterisks above the activity traces mark these peaks, asterisks below mark their onsets.
(B) SOM population activity plotted against PV population activity during the peaks identified in the same dataset depicted in A (red: PV events, blue: SOM events).
(C) Mean activity of the pyramidal population simultaneously imaged with the PV and SOM neurons in A-B, during PV events (red) and during SOM events (blue), z-scored.
(D) Same as C, but showing the mean activity of the PV population.
(E) Same as D, but showing the mean activity of the SOM population.
(F) Activity of the SOM, PV, and Pyr neurons from C-D, but overlaid and aligned only to the PV events. Right: Data from time marked by the arrow in F, normalized to max to show the timecourse. at event onset.
(G) As in F, but for SOM events.
(H) Pyr population activity trajectories through two dimensions of activity state space, for three example datasets. Dataset 1 is the same data as from A-G. Gray: activity preceding inhibitory events. Blue/Red: activity during inhibitory events (Blue: SOM events, Red: PV events). Black: activity after events. Thick lines: activity averaged across all population events. Thin lines: activity during individual events.
(I) Shared variability of the Pyr population in the first 25 eigenmodes identified with factor analysis, during SOM events (blue) and during PV events (red). *** p<0.0001. n = 6 datasets, with 10 random resamples of 75 Pyr neurons.

bioRxiv preprint doi: https://doi.org/10.1101/2023.01.09.523298; this version posted January 9, 2023. The copyright holder for this preprint (which was not certified by peer review) is the author/funder, who has granted bioRxiv a license to display the preprint in perpetuity. It is made available under aCC-BY-NC-ND 4.0 International license.

Discussion

Inhibitory interneurons, through their highly specialized connectivity motifs that include disinhibitory interactions, play unique functional roles in local cortical circuits (Pfeffer et al., 2013; Pi et al., 2013). However, the population-level interactions between inhibitory cell classes are difficult to predict from the 'average' wiring diagram of these neurons, and it is interactions between populations of neurons that process and transmit information in the brain. Here, we have implemented a method to easily allow simultaneous calcium imaging of two inhibitory neuron types, along with the rest of the neural population, *in vivo*. This methodology has allowed us to relate the activity of simultaneously imaged PV, SOM, and putative Pyr neurons in the posterior parietal cortex of mice. Inhibitory neurons in general were highly correlated with each other, and most strongly coordinated with other inhibitory neurons of the same type (Figure 3F). The functional interactions between Pyr neurons and inhibitory neurons degraded with distance, but the interactions among PV and SOM neurons remained strong for hundreds of microns (Figure 3G). Finally, we examined the activity patterns within the Pyr population that accompanied PV and SOM population activity events, and discovered that these were distinct: the patterns could be distinguished using dimensionality reduction methods, and the shared variability within the Pyr population was reduced during SOM events compared to PV events.

Other studies have measured activity in multiple inhibitory cell classes simultaneously in the cortex, but have mostly required technically challenging posthoc alignment of stained tissue (Kerlin et al., 2010; Khan et al., 2018b; Bugeon et al., 2022; Condylis et al., 2022). The methodology used here simply requires the cross-breeding of Cre- and Flp- driver mouse lines and the injection of a mixture of viruses to express spectrally separable fluorophores, but viruses with interneuron-specific promoters could also be used. A benefit is real-time knowledge of the cell type composition of imaging fields of view during acquisition, as a quick inspection of red fluorescence at short and long excitation wavelengths reveals mCherry vs tdTomato expressing neurons (Figure 1). Combining the current methods with posthoc staining and registration would allow further subdivisions of the broad PV, SOM, and VIP cell classes.

Our current results replicate and extend previous findings that activity within the inhibitory population tends to be highly correlated, but also that these correlations are even stronger among inhibitory neurons of the same type (Karnani et al., 2016; Khan et al., 2018a; Knoblich et al., 2019; Najafi et al., 2020; Bugeon et al., 2022; Khoury et al., 2022). Most of these studies were focused on sensory cortex, while here we have related SOM, PV, and Pyr activity in the posterior parietal cortex, an association-level area that receives convergent multimodal sensory input (Zingg et al., 2014; Song et al., 2017). The comparable results across studies suggest that strong functional connectivity within inhibitory cell classes is a generalizable feature of cortical circuits. Furthermore, we have demonstrated here that the correlations between Pyr neurons and other Pyr, PV, and SOM neurons decay with distance, but that the correlations among PV and SOM

bioRxiv preprint doi: https://doi.org/10.1101/2023.01.09.523298; this version posted January 9, 2023. The copyright holder for this preprint (which was not certified by peer review) is the author/funder, who has granted bioRxiv a license to display the preprint in perpetuity. It is made available under aCC-BY-NC-ND 4.0 International license.

neurons remain high for hundreds of microns. Future studies will determine the local circuit mechanisms producing these larger scale inhibitory networks, such as larger-scale and overlapping excitatory synaptic integration (Adesnik et al., 2012) or gap junctions within the inhibitory populations (Galarreta and Hestrin, 1999; Hu and Agmon, 2015).

The sizes of the neural populations we imaged, which include hundreds of putative Pyr neurons and tens of PV and SOM neurons, allowed us to study the population-level interactions between cell types. While the generalized wiring diagram of SOM and PV is known (Figure 1A), the resulting patterns of activity across the population cannot be easily predicted. We were able to identify activity events that were mostly restricted to one of the inhibitory subpopulations, either the PV or the SOM neurons. Interestingly, the temporal dynamics of activity in PV, SOM, and Pyr neurons that accompanied these events would be expected given the different sources of excitation to PV and SOM neurons. PV events were accompanied by synchronous activation of Pyr and PV neurons, while in SOM events, SOM activity followed activity of Pyr neurons. This insight is possible because we were able to compare activity of the same population of Pyr neurons to the activity states of two different inhibitory neuron types. Finally, dimensionality reduction tools revealed that distinct activity states of the pyramidal population were associated with SOM and PV events. Future work will determine the external inputs that trigger these activity events, and their effects on local processing.

Acknowledgments

This work was supported by the NIH Predoctoral Training Grant in Basic Neuroscience (T32 NS007433-21), Pew Biomedical Scholars Program, the Searle Scholars Program, the Klingenstein-Simons Fellowship Award in Neuroscience, and NIH grants NIMH DP2MH122404, NINDS R01NS121913. Judith Joyce Balcita-Pedicino performed histology and immunohistochemistry. We thank the GENIE project (Janelia) for making GCaMP sensors available for use. We thank the developers of Suite2P and Wavesurfer. pAAV-Ef1a-fDIO-mCherry was a gift from Karl Deisseroth (Addgene viral prep # 114471-AAV1). pAAV-FLEX-tdTomato was a gift from Edward Boyden (Addgene viral prep # 28306-AAV1). pAAV.Syn.GCaMP6f.WPRE.SV40 was a gift from Douglas Kim & GENIE Project (Addgene viral prep # 100837-AAV1). We thank Byron Yu for sharing the factor analysis code.

Author Contributions

C.T.P, C.D.B. and C.A.R. designed the experiments, C.T.P. and C.D.B. performed the experiments, C.T.P. and C.A.R. performed analyses, and C.T.P. and C.A.R. wrote the paper.

bioRxiv preprint doi: https://doi.org/10.1101/2023.01.09.523298; this version posted January 9, 2023. The copyright holder for this preprint (which was not certified by peer review) is the author/funder, who has granted bioRxiv a license to display the preprint in perpetuity. It is made available under aCC-BY-NC-ND 4.0 International license.

Methods

Animals

All procedures were approved by the University of Pittsburgh Institutional Animal Care and Use Committee. Homozygous SOM-Flp mice (Cat# 31629, Jackson Laboratory, USA) were crossed with homozygous PV-Cre mice (Cat# 17320, Jackson Laboratory, USA) obtained from, and all experiments were performed in the F1 generation, which expressed Flp in SOM+ neurons and Cre in PV + neurons. Mice were group housed in cages with between 2 and 4 mice. Adult (8–24 weeks) male and female mice were used for experiments (2 male, 1 female). Mice were housed on reversed 12 hr light/dark cycle, and all experiments were performed in the dark (active) phase.

Surgery

12-24 hours prior to surgery, mice were given a subcutaneous injection of dexamethasone (Covetrus, ME). Mice were anesthetized with isoflurane (4% for induction, 1-2% maintenance during surgery depending on breathing rate). Mice were mounted on a stereotaxic frame (David Kopf Instruments, CA). Subcutaneous injections of carprofen (Covetrus, ME) and dexamethasone were injected subcutaneously immediately prior to surgery for pain management and to reduce the inflammatory response. Ophthalmic ointment was applied to the eyes to prevent drying (Henry Schein, NY). A 3 x 3 mm craniotomy was made over PPC (centered at 2 mm posterior and 1.75 mm lateral to bregma) with a hand drill. A 1:1:2 mixture of three viruses was loaded into the glass injection pipet (1, Addgene #114471 pAAV-Ef1a-fDIO-mCherry, 2, Addgene #28306 pAAV-FLEX-tdTomato , and 3, Addgene #100837 pAAV.Syn.GCaMP6f.WPRE.SV40A). A micromanipulator (QUAD, Sutter, CA) was used to target injections ~250 μm under the dura at each site, where ~60 nL virus was pressure-injected over 5-10 minutes. Pipets were not removed until 5 minutes post-injection to prevent backflow. Dental cement (Parkell, NY) sealed a glass coverslip (3mm) over a drop of Kwik Sil (World Precision Instruments, FL) over the craniotomy. Using dental cement, a one-sided titanium headplate was attached to the right hemisphere of the skull. After mice had recovered from the anesthesia, they were returned to their home cages, and received oral carprofen tablets (Fisher Scientific, MA) for 3 days post-surgery.

Control Surgery

We performed our craniotomy surgery with the methods described above, except there were physically separated injections of the mCherry and tdTomato viral constructs at neighboring sites in each animal (six total injections). The mCherry virus was injected medially, while the tdTomato virus was injected laterally, with 1 mm separation in the mediolateral axis. The dilution of the virus was the same in all control and experimental animals, however one control animal received injections containing only the fluorophore viruses (diluted 1:10 with sterile 1X

bioRxiv preprint doi: https://doi.org/10.1101/2023.01.09.523298; this version posted January 9, 2023. The copyright holder for this preprint (which was not certified by peer review) is the author/funder, who has granted bioRxiv a license to display the preprint in perpetuity. It is made available under aCC-BY-NC-ND 4.0 International license.

PBS) while the other received control injections that also included the GCaMP virus (2:1:1 of GCaMP/red-expressing virus/PBS).

Two-photon microscope

Images were acquired using a resonant scanning two-photon microscope (Ultima Investigator, Bruker, WI) at a 30 Hz frame rate and 512 x 512 pixel resolution through a 16x water immersion lens. PPC was imaged at a depth between 150 and 250 μm, at the level cortical layer 2/3. The angle of the objective was matched to the angle of the window. Excitation light was provided by both a tunable femtosecond infrared source (780-1100 nm) and a fixed 1045 nm wavelength laser (Insight X3, Spectra-Physics, CA). Tunable and fixed wavelength beams were combined with a dichroic mirror (ZT1040dcrb-UF3, Chroma, VT) before being routed to the microscope's galvanometers. Note that because of this optics configuration, imaging cannot be performed at tunable wavelengths immediately surrounding 1045 nm. Green and red wavelengths were separated through a 565 nm lowpass filter before passing through bandpass filters (Chroma, ET525/70 and ET 595/50, VT). PrairieView software (vX5.5 Bruker, WI) was used to control the microscope.

Behavioral Monitoring

Running velocity was monitored on pitch, roll, and yaw axes using two optical sensors (ADNS-98000, Tindie, CA) held adjacent to the spherical treadmill. A microcontroller (Teensy, 3.1, Adafruit, NY) communicated with the sensors, demixing their inputs to produce one output channel per rotational axis using custom code. Outputs controlling the galvanometers were synchronized with running velocity using a digital oscilloscope (DIGIDATA 155080, pClamp 11, Molecular Devices). Instantaneous velocity was calculated using the distance formula, using pitch and roll velocity values as inputs.

Image Acquisition

Fields of view were selected based on GCaMP expression and red fluorophore expression. mCherry vs tdTomato expression could be quickly assessed by comparing images collected at 780 nm and 1045 nm excitation, as both fluorophores were visible at 1045 nm, but only mCherry was visible at 780 nm. Multiple imaging sessions were acquired from each cranial window, varying depths and locations rostro-caudally and medio-laterally. The wavelength series to distinguish mCherry and tdTomato fluorescence was performed first. Images were collected at excitation wavelengths from 780 nm to 1100 nm in increments of 20 nm each averaged over 16 frames, excluding 1020 and 1060 nm wavelengths (see *Two photon microscope*). The 1045 nm image was acquired with the fixed-wavelength beam from the Insight laser. At each wavelength, images were taken at multiple powers (0 to 275 mW). The laser was then tuned to 920 nm for functional imaging of GCaMP fluorescence. Images were collected while mice ran voluntarily on an air-suspended spherical treadmill (Khoury et al., 2022). Functional imaging sessions were approximately 30 minutes in duration. All images were collected at a 30 Hz frame rate.

bioRxiv preprint doi: https://doi.org/10.1101/2023.01.09.523298; this version posted January 9, 2023. The copyright holder for this preprint (which was not certified by peer review) is the author/funder, who has granted bioRxiv a license to display the preprint in perpetuity. It is made available under aCC-BY-NC-ND 4.0 International license.

Image Processing

The images from the wavelength series and functional imaging were processed separately in Suite2p (v0.10.3) in Python with Cellpose (v0.7.3), along with 1000 frames of images from collected during the functional imaging phase of the same imaging session, to allow for registration between the wavelength series and the functional imaging. The suite2p software registered these images to correct for brain motion. Motion correction was performed on the functional images collected at 920 nm and on the wavelength series, only the functional imaging was used for ROI extraction. Custom MATLAB code was used to load the two registered series of images. Any discrepancy in registration between these two datasets was corrected by adding the peak lag of the cross correlation between the wavelength series and functional data in the X and Y directions to the coordinates of the ROIs. This correction was manually verified by plotting the circumference of the ROIs over the mean images from each image registration and confirming that the location of the ROIs relative to the cells were identical.

We then manually selected which of the ROIs generated from the functional imaging that corresponded to cells expressing a red fluorophore. To rule out potentially ambiguous red neurons, we plotted the ROI outlines onto the max projection of the wavelength series, as well as mean images taken from the 780-820nm range and the 960-1045nm range. Any ROI containing out of focus red expression or that contained overlapping red neuropil or a closely neighboring soma from another neuron was excluded from analysis entirely. Vectors were generated for each of the red fluorophore containing cells, where each dimension was the mean intensity of the pixels of each cells ROI at a given wavelength.

For the control data (Figure 1), since there was no functional data to generate ROIs in suite2p, ROIs were manually drawn.

mCherry and tdTomato ROI Classification

The Vectors containing the mean intensity of all pixels for each ROI at each wavelength (see *Image Processing*) were run through the k-means clustering algorithm function in MATLAB. This algorithm uses a squared Euclidian distance metric for optimization and the k-means++ algorithm for cluster center initialization. Silhouette scores were calculated for each neuron using the following formula:

SS = (distance to other centroid – distance to own centroid)/max (distance own, distance other)

The k-means clustering algorithm was applied to every possible combination of imaging wavelengths (n=32752 combinations) described above on each of the 6 datasets from our control animals. We used the mean of the silhouette scores for all neurons in each iteration of this process as a metric of cluster separability. For all subsequent analyses, we used a specific wavelength combination that performed well across all control datasets, to maximize the stability of classification across datasets (780, 800, 820, 940, 960 nm). To determine a threshold by

bioRxiv preprint doi: https://doi.org/10.1101/2023.01.09.523298; this version posted January 9, 2023. The copyright holder for this preprint (which was not certified by peer review) is the author/funder, who has granted bioRxiv a license to display the preprint in perpetuity. It is made available under aCC-BY-NC-ND 4.0 International license.

which cells would be excluded, we examined the distribution of silhouette scores of misclassified cells from all the iterations of clustering on control data. Note that these included 'suboptimal' combinations of wavelengths that do not distinguish mCherry and tdTomato as well. The silhouette scores from the bottom 10% of these iterations were excluded, as quantified by number of cells misclassified. This was done to remove confounding datasets where clustering was unlikely to be related to the separability of datasets. We took two standard deviations above the mean of this distribution as a threshold for exclusion (0.7 SS). Any neuron in our experimental data that had a silhouette score lower than this value was excluded from analysis entirely. The cluster that included ROIs with strong fluorescence at 780 nm was identified as the mCherry/SOM cluster.

GCaMP Fluorescence Processing

Images of GCaMP fluorescence collected with 920 nm excitation were processed in a separate suite2p instance (v 0.10.3, Cellpose 0.7.3). Raw imaging movies were processed to correct for motion, identify cell bodies, and extract soma and neuropil fluorescence. Suite2p generated regions of interests (ROIs) for each cell based on anatomical features and correlations between pixels across time during functional imaging. ROIs were manually verified to be cell bodies, as opposed to dendritic processed, based on their morphology. The fluorescence of the neuropil surrounding the cell body was subtracted off from the fluorescence of the cell body, weighted by a factor of .7. The resulting signal was used for extracting a dF/F and deconvolved signal for each cell. ROIs classified as mCherry+ were considered SOM neurons, tdTomato+ were considered PV neurons, and GCaMP+ neurons that had no red fluorescence were considered putative pyramidal (Pyr) neurons, these neurons comprise >90% of cortical neurons that do not express PV or SOM(Tremblay et al., 2016).

dF/F and Deconvolution

Once the neuropil corrected fluorescence was obtained for each animal (F), dF/F was calculated for each neuron (F-Fbaseline)/Fbaseline for each frame. Fbaseline was the eighth percentile of the 900 F values surrounding that frame for a given neuron (~15 s in each direction, 30 s total). dF/F timeseries were then deconvolved to estimate the relative spike rate in each imaging frame using the OASIS toolbox. We used the AR1 FOOPSI algorithm and allowed the toolbox to optimize the convolution, kernel, baseline fluorescence, and noise distribution. All events below a threshold of .05 au were removed from analysis.

Pairwise correlations

Partial Pearson correlations were computed between all pairs of neurons, for all combinations of cell types: Pyr-Pyr, SOM-SOM, PV-PV, Pyr-SOM, Pyr-PV, SOM-PV. Activity was smoothed in time (300 ms), and the partial Pearson correlation between the activity of the neurons was computed, discounting the effect of lateral running speed (Matlab function 'partialcorr'). To

bioRxiv preprint doi: https://doi.org/10.1101/2023.01.09.523298; this version posted January 9, 2023. The copyright holder for this preprint (which was not certified by peer review) is the author/funder, who has granted bioRxiv a license to display the preprint in perpetuity. It is made available under aCC-BY-NC-ND 4.0 International license.

relate the relationship between Pearson correlation and inter-somatic distance by cell type, all pairwise Pearson correlations for each combination were pooled across datasets and z-scored.

Identification of PV and SOM population events

Coordinated PV and SOM events were identified for each imaging session as follows. For each interneuron population, the activity of the individual neurons was z-scored over its entire time series and averaged across neurons. This neuron-averaged time-series was then z-scored. Peaks in this population activity signal were identified (MATLAB's function 'findpeaks', MinPeakHeight: 2 standard deviations, MinPeakDistance: 2 s MinPeakProminence: 2 standard deviations). Peaks in each interneuron population were discarded if they corresponded to elevated activity in the other interneuron population (> 2 standard deviations). The onset of the population activity events was defined as the last time preceding the peak where the z-scored activity was less than 0.

Population-level interactions

Factor analysis was applied to visualize the patterns of Pyr population activity in high dimensional space, and to measure the shared variability (Yu et al., 2009; Huang et al., 2019). The deconvolved responses of a randomly selected subset of 75 Pyr neurons within each imaging session were binned (~66 ms bins). Factor analysis was applied to collect the first 40 latent factor, separately activity surrounding PV and SOM events (4 s before and after event onsets). The eigenvalue for each latent factor corresponds to the Pyr population's shared variability in that dimension. This procedure was repeated 10 times for each dataset.

Histology

After all imaging sessions had been acquired, each mouse was transcardially perfused with saline and then 4% paraformaldehyde. The brain was extracted, cryoprotected, embedded, frozen, and sliced. Once slide mounted, we stained brains with DAPI to be able to identify structure. We used anatomical structure to verify the locations of our injections in PPC.

bioRxiv preprint doi: https://doi.org/10.1101/2023.01.09.523298; this version posted January 9, 2023. The copyright holder for this preprint (which was not certified by peer review) is the author/funder, who has granted bioRxiv a license to display the preprint in perpetuity. It is made available under aCC-BY-NC-ND 4.0 International license.

Table 1 Pairwise Correlations from Figure 3.

	Pair Type	Mean	std	n pairs
1	PV-PV	0.0656	0.1148	5702
2	SOM-SOM	0.0761	0.1229	594
3	Pyr-Pyr	0.0199	0.0504	317022
4	PV-SOM	0.0417	0.083	955
5	PV-Pyr	0.0327	0.0621	25581
6	SOM-Pyr	0.0241	0.0628	16303
	permutation tests	wilcoxon		
1 vs 2	0.034	0.6131		
1 vs 3	9.99E-04	<.000000001		
1 vs 4	9.99E-04	<.000000001		
1 vs 5	9.99E-04	<.000000001		
1 vs 6	9.99E-04	<.000000001		
2 vs 3	9.99E-04	<.000000001		
2 vs 4	9.99E-04	<.000000001		
2 vs 5	9.99E-04	<.000000001		
2 vs 6	9.99E-04	<.000000001		
3 vs 4	9.99E-04	<.000000001		
3 vs 5	9.99E-04	1		
3 vs 6	9.99E-04	0.0079		
4 vs 5	9.99E-04	0.005		
5 vs 6	9.99E-04	<.000000001		

bioRxiv preprint doi: https://doi.org/10.1101/2023.01.09.523298; this version posted January 9, 2023. The copyright holder for this preprint (which was not certified by peer review) is the author/funder, who has granted bioRxiv a license to display the preprint in perpetuity. It is made available under aCC-BY-NC-ND 4.0 International license.

Table 2: Relationship between Pairwise Correlation and Distance, From Figure 3

PV-PV	0.1159
SOM-SOM	0.0699
Pyr-Pyr	9.99E-04
PV-SOM	0.2348
PV-Pyr	9.99E-04
SOM-Pyr	9.99E-04

bioRxiv preprint doi: https://doi.org/10.1101/2023.01.09.523298; this version posted January 9, 2023. The copyright holder for this preprint (which was not certified by peer review) is the author/funder, who has granted bioRxiv a license to display the preprint in perpetuity. It is made available under aCC-BY-NC-ND 4.0 International license.

References

Adesnik H, Bruns W, Taniguchi H, Huang ZJ, Scanziani M (2012) A neural circuit for spatial summation in visual cortex. Nature 490:226–231.

Atallah BV, Bruns W, Carandini M, Scanziani M (2012) Parvalbumin-expressing interneurons linearly transform cortical responses to visual stimuli. Neuron 73:159–170 Available at: http://eutils.ncbi.nlm.nih.gov/entrez/eutils/elink.fcgi?dbfrom=pubmed&id=22243754&retmode=ref&cmd=prlinks.

Bugeon S, Duffield J, Dipoppa M, Ritoux A, Prankerd I, Nicoloutsopoulos D, Orme D, Shinn M, Peng H, Forrest H, Viduolyte A, Reddy CB, Isogai Y, Carandini M, Harris KD (2022) A transcriptomic axis predicts state modulation of cortical interneurons. Nature 607:330–338.

Cardin JA, Carlén M, Meletis K, Knoblich U, Zhang F, Deisseroth K, Tsai L-H, Moore CI (2009) Driving fast-spiking cells induces gamma rhythm and controls sensory responses. Nature 459:663–667 Available at: http://www.nature.com/nature/journal/vaop/ncurrent/full/nature08002.html.

Chen N, Sugihara H, Sur M (2015) An acetylcholine-activated microcircuit drives temporal dynamics of cortical activity. Nature Neuroscience 18:892–902.

Chen T-W, Wardill TJ, Sun Y, Pulver SR, Renninger SL, Baohan A, Schreiter ER, Kerr RA, Orger MB, Jayaraman V, Looger LL, Svoboda K, Kim DS (2013) Ultrasensitive fluorescent proteins for imaging neuronal activity. Nature 499:295–300.

Condylis C, Ghanbari A, Manjrekar N, Bistrong K, Yao S, Yao Z, Nguyen TN, Zeng H, Tasic B, Chen JL (2022) Dense functional and molecular readout of a circuit hub in sensory cortex. Science 375:eabl5981.

Cunningham JP, Yu BM (2014) Dimensionality reduction for large-scale neural recordings. Nat Neurosci 17:1500–1509.

Dipoppa M, Ranson A, Krumin M, Pachitariu M, Carandini M, Harris KD (2018) Vision and Locomotion Shape the Interactions between Neuron Types in Mouse Visual Cortex. Neuron 98:602-615.e8.

Drobizhev M, Tillo S, Makarov NS, Hughes TE, Rebane A (2009) Absolute two-photon absorption spectra and two-photon brightness of orange and red fluorescent proteins. The journal of physical chemistry B 113:855–859 Available at: http://pubs.acs.org/doi/abs/10.1021/jp8087379.

Fanselow EE, Richardson KA, Connors BW (2008) Selective, state-dependent activation of somatostatin-expressing inhibitory interneurons in mouse neocortex. Journal of

bioRxiv preprint doi: https://doi.org/10.1101/2023.01.09.523298; this version posted January 9, 2023. The copyright holder for this preprint (which was not certified by peer review) is the author/funder, who has granted bioRxiv a license to display the preprint in perpetuity. It is made available under aCC-BY-NC-ND 4.0 International license.

neurophysiology 100:2640–2652 Available at: http://jn.physiology.org/cgi/content/full/100/5/2640.

Galarreta M, Hestrin S (1999) A network of fast-spiking cells in the neocortex connected by electrical synapses. Nature 402:72–75.

Garcia-Junco-Clemente P, Ikrar T, Tring E, Xu X, Ringach DL, Trachtenberg JT (2017) An inhibitory pull-push circuit in frontal cortex. Nat Neurosci 20:389–392.

Hofer SB, Ko H, Pichler B, Vogelstein J, Ros H, Zeng H, Lein E, Lesica NA, Mrsic-Flogel TD (2011) Differential connectivity and response dynamics of excitatory and inhibitory neurons in visual cortex. Nature Neuroscience 14:1045–1052 Available at: http://eutils.ncbi.nlm.nih.gov/entrez/eutils/elink.fcgi?dbfrom=pubmed&id=21765421&retmode=ref&cmd=prlinks.

Hu H, Agmon A (2015) Properties of precise firing synchrony between synaptically coupled cortical interneurons depend on their mode of coupling. J Neurophysiol 114:624–637.

Huang C, Ruff DA, Pyle R, Rosenbaum R, Cohen MR, Doiron B (2019) Circuit Models of Low-Dimensional Shared Variability in Cortical Networks. Neuron 101:337-348.e4 Available at: https://www.sciencedirect.com/science/article/pii/S0896627318310432.

Karnani MM, Jackson J, Ayzenshtat I, Tucciarone J, Manoocheri K, Snider WG, Yuste R (2016) Cooperative Subnetworks of Molecularly Similar Interneurons in Mouse Neocortex. Neuron 90:86–100 Available at: https://ac.els-cdn.com/S0896627316001744/1-s2.0-S0896627316001744-main.pdf?_tid=bcdbac52-756f-4d9d-b79f-986ba82d1b59&acdnat=1534005358_d3924971dcdde262b89985a0ce1778a5.

Kato HK, Asinof SK, Isaacson JS (2017) Network-Level Control of Frequency Tuning in Auditory Cortex. Neuron 95:412-423.e4.

Kerlin AM, Andermann ML, Berezovskii VK, Reid RC (2010) Broadly tuned response properties of diverse inhibitory neuron subtypes in mouse visual cortex. Neuron 67:858–871 Available at: http://www.sciencedirect.com/science?_ob=ArticleURL&_udi=B6WSS-50YV1JT-N&_user=501045&_coverDate=09%2F09%2F2010&_rdoc=1&_fmt=high&_orig=search&_origin=search&_sort=d&_docanchor=&view=c&_acct=C000022659&_version=1&_urlVersion=0&_userid=501045&md5=c60cf995542c121c173f5c038760c07e&searchtype=a.

Khan AG, Poort J, Chadwick A, Blot A, Sahani M, Mrsic-Flogel TD, Hofer SB (2018a) Distinct learning-induced changes in stimulus selectivity and interactions of GABAergic interneuron classes in visual cortex. Nature Neuroscience 21:851–859.

Khan AG, Poort J, Chadwick A, Blot A, Sahani M, Mrsic-Flogel TD, Hofer SB (2018b) Distinct learning-induced changes in stimulus selectivity and interactions of GABAergic interneuron

bioRxiv preprint doi: https://doi.org/10.1101/2023.01.09.523298; this version posted January 9, 2023. The copyright holder for this preprint (which was not certified by peer review) is the author/funder, who has granted bioRxiv a license to display the preprint in perpetuity. It is made available under aCC-BY-NC-ND 4.0 International license.

classes in visual cortex. Nature Neuroscience 21:851–859 Available at: https://www.nature.com/articles/s41593-018-0143-z.

Khoury CF, Fala NG, Runyan CA (2022) The spatial scale of somatostatin subnetworks increases from sensory to association cortex. Cell Reports 40:111319.

Knoblich U, Huang L, Zeng H, Li L (2019) Neuronal cell-subtype specificity of neural synchronization in mouse primary visual cortex. Nat Commun 10:2533.

Kuchibhotla KV, Gill JV, Lindsay GW, Papadoyannis ES, Field RE, Sten TAH, Miller KD, Froemke RC (2016) Parallel processing by cortical inhibition enables context-dependent behavior. Nature Neuroscience Available at: http://www.nature.com/neuro/journal/vaop/ncurrent/full/nn.4436.html.

Levy RB, Reyes AD (2012) Spatial profile of excitatory and inhibitory synaptic connectivity in mouse primary auditory cortex. J Neurosci Official J Soc Neurosci 32:5609–5619.

Musall S, Kaufman MT, Juavinett AL, Gluf S, Churchland AK (2019) Single-trial neural dynamics are dominated by richly varied movements. Nat Neurosci 22:1677–1686.

Najafi F, Elsayed GF, Cao R, Pnevmatikakis E, Latham PE, Cunningham JP, Churchland AK (2020) Excitatory and Inhibitory Subnetworks Are Equally Selective during Decision-Making and Emerge Simultaneously during Learning. Neuron 105:165-179.e8.

Pfeffer CK, Xue M, He M, Huang ZJ, Scanziani M (2013) Inhibition of Inhibition in Visual Cortex: The Logic of Connections Between Molecularly Distinct Interneurons. Nat Neurosci 16:1068–1076.

Pfeffer T, Keitel C, Kluger DS, Keitel A, Russmann A, Thut G, Donner TH, Gross J (2022) Coupling of pupil- and neuronal population dynamics reveals diverse influences of arousal on cortical processing. Elife 11:e71890.

Pi H-J, Hangya B, Kvitsiani D, Sanders JI, Huang ZJ, Kepecs A (2013) Cortical interneurons that specialize in disinhibitory control. Nature 503:521–524.

Poort J, Khan AG, Pachitariu M, Nemri A, Orsolic I, Krupic J, Bauza M, Sahani M, Keller GB, Mrsic-Flogel TD, Hofer SB (2015) Learning Enhances Sensory and Multiple Non-sensory Representations in Primary Visual Cortex. Neuron 86:1478–1490.

Rikhye RV, Yildirim M, Hu M, Breton-Provencher V, Sur M (2021) Reliable sensory processing in mouse visual cortex through cooperative interactions between somatostatin and parvalbumin interneurons. J Neurosci:JN-RM-3176-20.

Sohal VS, Zhang F, Yizhar O, Deisseroth K (2009) Parvalbumin neurons and gamma rhythms enhance cortical circuit performance. Nature 459:698–702 Available at: http://www.nature.com/nature/journal/v459/n7247/full/nature07991.html.

bioRxiv preprint doi: https://doi.org/10.1101/2023.01.09.523298; this version posted January 9, 2023. The copyright holder for this preprint (which was not certified by peer review) is the author/funder, who has granted bioRxiv a license to display the preprint in perpetuity. It is made available under aCC-BY-NC-ND 4.0 International license.

Song S, Sjöström PJ, Reigl M, Nelson S, Chklovskii DB (2005) Highly nonrandom features of synaptic connectivity in local cortical circuits. PLoS Biology 3:e68 Available at: http://eutils.ncbi.nlm.nih.gov/entrez/eutils/elink.fcgi?dbfrom=pubmed&id=15737062&retmode=ref&cmd=prlinks.

Song Y-H, Kim J-H, Jeong H-W, Choi I, Jeong D, Kim K, Lee S-H (2017) A Neural Circuit for Auditory Dominance over Visual Perception. Neuron 93:940-954.e6.

Stringer C, Pachitariu M, Steinmetz N, Reddy CB, Carandini M, Harris KD (2019) Spontaneous behaviors drive multidimensional, brainwide activity. Science 364:eaav7893.

Tremblay R, Lee S, Rudy B (2016) GABAergic Interneurons in the Neocortex: From Cellular Properties to Circuits. Neuron 91:260–292 Available at: http://www.sciencedirect.com/science/article/pii/S0896627316303117.

Veit J, Hakim R, Jadi MP, Sejnowski TJ, Adesnik H (2017) Cortical gamma band synchronization through somatostatin interneurons. Nature Neuroscience 20:951–959.

Wang X-J, Yang GR (2018) A disinhibitory circuit motif and flexible information routing in the brain. Curr Opin Neurobiol 49:75–83.

Wehr M, Zador AM (2003) Balanced inhibition underlies tuning and sharpens spike timing in auditory cortex. Nature 426:442–446 Available at: http://eutils.ncbi.nlm.nih.gov/entrez/eutils/elink.fcgi?dbfrom=pubmed&id=14647382&retmode=ref&cmd=prlinks.

Wilson NR, Runyan CA, Wang FL, Sur M (2012) Division and subtraction by distinct cortical inhibitory networks in vivo. Nature 488:343–348 Available at: http://eutils.ncbi.nlm.nih.gov/entrez/eutils/elink.fcgi?dbfrom=pubmed&id=22878717&retmode=ref&cmd=prlinks.

Yoshimura Y, Callaway EM (2005) Fine-scale specificity of cortical networks depends on inhibitory cell type and connectivity. Nature Neuroscience 8:1552–1559 Available at: http://www.nature.com/doifinder/10.1038/nn1565.

Yu BM, Cunningham JP, Santhanam G, Ryu SI, Shenoy KV, Sahani M (2009) Gaussian-Process Factor Analysis for Low-Dimensional Single-Trial Analysis of Neural Population Activity. Journal of neurophysiology 102:614–635.

Zingg B, Hintiryan H, Gou L, Song MY, Bay M, Bienkowski MS, Foster NN, Yamashita S, Bowman I, Toga AW, Dong H-W (2014) Neural networks of the mouse neocortex. Cell 156:1096–1111.

Znamenskiy P, Kim M-H, Muir DR, Iacaruso MF, Hofer SB, Mrsic-Flogel TD (2018) Functional selectivity and specific connectivity of inhibitory neurons in primary visual cortex. Biorxiv:294835.

bioRxiv preprint doi: https://doi.org/10.1101/2023.01.09.523298; this version posted January 9, 2023. The copyright holder for this preprint (which was not certified by peer review) is the author/funder, who has granted bioRxiv a license to display the preprint in perpetuity. It is made available under aCC-BY-NC-ND 4.0 International license.